




PAPER

[View Article Online](#)
[View Journal](#) | [View Issue](#)Cite this: *J. Mater. Chem. A*, 2025, 13, 39903

A fluorine-free Li-ion battery features comparable cycling performance to a highly-fluorinated equivalent

Saeed Mardi,  Andrew J. Naylor,  Jonas Mindemark 
and Guiomar Hernández *

Fluorinated compounds, including the polyvinylidene fluoride (PVdF) binder and lithium hexafluorophosphate salt, are considered essential components in lithium-ion batteries due to their ability to provide good performance and cycle life. However, these compounds raise potential environmental concerns, as they can lead to the formation of toxic, corrosive and persistent compounds, such as hydrofluoric acid, phosphorus pentafluoride (PF₅) and per- and polyfluoroalkyl substances. In this study, the effects of a fluorine-free electrolyte consisting of lithium bis(oxalato)borate (LiBOB) salt with the vinylene carbonate (VC) additive, and an aqueous-based binder based on carboxymethyl cellulose (CMC) and latex are investigated for full cells combining a silicon-graphite composite anode with LiNi_{0.6}Mn_{0.2}Co_{0.2}O₂ (NMC622) cathodes. Higher capacity retention is obtained at C/2 after 500 cycles with the fluorine-free binder in the cathode (61% and 65% for the fluorine-free and fluorinated electrolytes, respectively) compared to the PVdF-based binder (58% and 56%, respectively). X-ray photoelectron spectroscopy analysis of the passivating layers on the cathode and anode across the four systems revealed a F-rich interfacial composition in the presence of the fluorinated electrolyte, while the fluorine-free electrolyte led to the formation of oxygen-rich layers at the interphases. Despite the chemical differences, both layers protect the cathode and anode during cycling, resulting in similar electrochemical performance. Moreover, the solid electrolyte interphase composition on the anode is dependent on the cathode's formulation. The aqueous-processed cathode resulted in higher coverage of the active material, which mitigated salt decomposition and facilitated the formation of a more stable passivating layer. This contributed to higher capacity retention despite a lower initial discharge capacity compared to the PVdF-based cathode. This study demonstrates the potential of fluorine-free components (electrolyte and a binder with an aqueous-processed cathode) to achieve high-energy-density full cells with comparable performance to conventional highly fluorinated lithium-ion batteries.

Received 20th August 2025
Accepted 21st October 2025

DOI: 10.1039/d5ta06760j

rsc.li/materials-a

Introduction

The global shift toward decarbonisation and electrification of transportation entails a large production of energy storage devices. During this transition, technology advancement should not solely prioritize energy density and cycle life; ecological production, battery recycling, cost and safety are also critical to consider.¹ In this context, regulations are coming strong, for example, requiring higher amount of recycled materials to be used in batteries and the proposal to ban the use of per- and polyfluoroalkyl substances (PFAS) in the European Union from the European Chemicals Agency (ECHA).^{2,3} In lithium-ion batteries (LIBs), PFAS and other fluorinated compounds are mainly found in binders and electrolytes. While fluorinated compounds are currently considered essential for good battery

performance, they pose many challenges for the environment and during battery recycling as they remain as impurities in the recycled products.² Therefore, the search for fluorine-free alternatives is more pressing than ever.⁴

In addition to LIBs, recent advancements in fluorine-free materials have demonstrated promising implementation across a range of energy storage and conversion devices beyond LIBs, for instance, electrolytes in supercapacitors,⁵ and membranes in redox flow batteries,⁶ fuel cells,⁷ and water electrolysis.⁸

High voltage cathode materials, especially those with high nickel content, still rely on PFAS-based binders, such as polyvinylidene fluoride (PVdF). Besides the source of PFAS, this binder has other environmental impacts worth highlighting. The first is the use of *N*-methyl-2-pyrrolidone (NMP) solvent, which is harmful to the environment and humans, requiring solvent recovery during drying. Second, due to the high boiling point of NMP (202 °C), elevated temperatures are required for

Department of Chemistry – Ångström Laboratory, Uppsala University, Uppsala, SE-751 21, Sweden. E-mail: guiomar.hernandez@kemi.uu.se



the drying of electrodes which makes the process less energy efficient, and increases the overall production cost. Therefore, cathode electrode fabrication is transitioning towards fluorine-free aqueous-processed binders to reduce the environmental impact and facilitate the large-scale production of more sustainable and cheaper lithium-ion batteries (LIBs).⁹ Examples of fluorine-free binders for NMC-based cathodes include polyacrylic acid (PAA),¹⁰ sodium carboxymethyl cellulose (CMC),¹¹ CMC-latex,^{12,13} and carrageenan biopolymers.¹⁴

Another source of fluorinated compounds in batteries is the electrolyte composed of fluorinated salts and additives, such as LiPF₆ and fluoroethylene carbonate (FEC). Even if they do not fall into the PFAS category and regulations, they can react and degrade to release toxic and corrosive compounds (HF and PF₅), posing risks during manufacturing, accidents and battery dismantling and recycling.^{2,15} Furthermore, they are detrimental to the recycling process as they corrode the reactors and leave fluorine as an impurity in the recycled products. Therefore, switching to fluorine-free alternative electrolytes is another approach towards realizing more sustainable and environmentally friendly batteries. However, it is worth noting that, to the best of our knowledge, life cycle assessments of fluorine-free electrolyte alternatives have not been done yet to confirm this.

In recent decades, several fluorine-free salts such as lithium bis(glycolato)borate (BGB),¹⁶ lithium perchlorate (LiCl₄),¹⁷ and lithium nitrate (LiNO₃)¹⁸ have been proposed for LIBs.¹⁹ Among them, lithium bis(oxalato)borate (LiBOB) is the most studied case. However, none of them have reached their commercialization yet. The most widespread use of LiBOB is as an additive in electrolytes, to passivate the electrode surface and facilitate the formation of CEI and SEI layers.^{20–22} The main drawbacks of using LiBOB as the main salt include its lower solubility and ionic conductivity compared to the fluorinated electrolyte salts (0.8 M and 8–9 mS cm^{−1} vs. >1 M and >10 mS cm^{−1}, respectively).²³ Despite these limitations, promising electrochemical performance has been reported with fluorine-free electrolytes based on LiBOB when using graphite-based anodes with various Co-poor and Co-free cathodes.^{24–27}

For the next generation of LIBs, low-cobalt- and high-nickel-content cathode materials, along with silicon-based anodes, have garnered significant attention. Higher Ni content in LiNi_xMn_yCo_{1−x−y}O₂ materials provides higher reversible capacity at the same cut-off voltage. However, it brings other issues such as higher sensitivity toward moisture and oxidation/decomposition of the electrolyte at the interface. The primary motivation for the development of Si-based anodes is their higher theoretical capacity compared to the conventional graphite anode (3579 mA h g^{−1} vs. 372 mA h g^{−1}, respectively). However, their application is limited due to rapid capacity fading, primarily attributed to consecutive volume changes of Si during lithiation/delithiation cycles. Recently, the effect of electrolyte fluorination on Si-graphite||NMC111 full cells with high mass loading electrodes has been investigated.²⁷ A fluorine-free electrolyte based on LiBOB and the VC additive showed similar cycling performance at low current densities compared to the highly fluorinated analogue; however, the performance was limited at high current densities.

Furthermore, the choice of the binder and active material (graphite–silicon) affects the SEI properties and, therefore, can have implications on its stability and subsequent cell performance.^{28–30}

Herein, we have employed a fluorine-free electrolyte based on LiBOB salt and the VC additive in full cells containing high-mass-loading and high-energy-density electrodes of a graphite–silicon alloy as the anode and NMC622 as the cathode paired with fluorinated and fluorine-free binders. The electrochemical performance of these cells has been investigated and correlated with the morphology and chemical composition of the anode's and cathode's interphases to understand their formation and stability upon long-term cycling. This study provides a pathway toward competitive fluorine-free lithium-ion batteries compared to the state of the art, bringing us closer to the realization of more sustainable and environmentally friendly energy storage solutions.

Experimental

Materials and methods

Materials. LP57 electrolyte (SelectiLyte BASF, 1 M LiPF₆, ethylene carbonate (EC)/ethyl methyl carbonate (EMC) 3 : 7 v/v), EC (SelectiLyte BASF), EMC (SelectiLyte BASF), dimethyl carbonate (DMC, anhydrous ≥99%, Sigma-Aldrich), vinylene carbonate (VC, SelectiLyte BASF), and fluoroethylene carbonate (FEC, Gotion) were battery-grade and used as received. Lithium bis(oxalato)borate (LiBOB, Chemetall) was dried at 120 °C for 12 h under vacuum prior to electrolyte preparation.

Electrodes. Silicon–graphite electrodes were kindly provided by VARTA Innovation GmbH. These were composed of a silicon alloy (L-20772, provided by 3 M), graphite (BTR 918), Super-P carbon black and the lithium polyacrylate (LiPAA, 450 K) binder in a mass ratio of 25 : 66 : 2 : 7 and an areal capacity of 2.4 mA h cm^{−2}. Organic-based NMC622 cathodes with the PVdF binder were kindly provided by VARTA Innovation GmbH with an areal capacity of 2.2 mA h cm^{−2}. Aqueous-processed NMC622 cathodes were kindly provided by CEA-Liten with an electrode mass loading of 11.6 mg cm^{−2} and an areal capacity of 1.9 mA h cm^{−2} using 180 mA h g^{−1} specific capacity for the NMC622 cathode material. The composition of the latter was 92 wt% NMC622, 4 wt% carbon black, 1 wt% CMC and 3 wt% latex and it was coated onto carbon-coated aluminium foil (from Armor). The N : P ratios for organic-based and aqueous-processed NMC622 cathodes are 1.09 and 1.26, respectively. Electrodes were cut in Ø13 mm discs and dried at 120 °C under vacuum for 12 h.

Cell assembly and testing. The fluorinated electrolyte was prepared by adding 10 vol% FEC and 2 vol% VC to LP57. The fluorine-free electrolyte was prepared by mixing LiBOB in EC/EMC 3 : 7 v/v with a molal concentration of 0.7 and adding 2 vol% VC. Two-electrode full cells were assembled in coin cells in an argon glovebox with a Ø17 mm Celgard 2325 separator and 50 µL of electrolyte. Three-electrode cells were assembled in pouch cells using lithium metal foil as the reference electrode (ring shape with inner and outer diameters of 16 and 22 mm, respectively), a Ø25 mm Celgard 2325 separator and 120 µL of



electrolyte. The reference electrode was placed between the working and counter electrodes with separators on both sides. The cells rested for 6 h before cycling was initiated.

Galvanostatic cycling of NMC622/Si-graphite full cells was performed at room temperature using an Arbin BT-2043 battery testing system. The C-rate used for cycling was based on the cathode's reversible capacity provided by the suppliers stated above. For NMC622 cathodes with the PVdF binder, the initial two cycles were done at C/20 between 3.0 and 4.2 V with a constant voltage step at the end of the charge step until the current dropped to C/50. Afterwards, the cells were cycled at C/2 with a constant voltage at the charge state until the current was below C/20. For the aqueous-processed one, the same protocol was applied without the constant voltage step. The intermittent current interruption (ICI) method consisting of 1 s rest at 5 min intervals was used to determine the internal cell resistance following the analysis procedure reported by Lacey *et al.*³¹ and Chien *et al.*³² C-rate capability tests were performed at C/10, C/5, C/2, 1C, 2C and C/2 for five cycles at each current density. Areal capacities were used to calculate the current.

Surface analysis. Prior to surface analysis, cells were disassembled in an argon glovebox and the electrodes were removed and rinsed with 2 mL of dimethyl carbonate. For SEM/EDS, the samples were transferred to a vacuum-sealed transfer chamber and measured with a field-emission scanning electron microscope (Merlin, Carl Zeiss, Germany) with an acceleration voltage of 3 kV and a beam current of 100 pA. EDS was measured with an acceleration voltage of 15 kV and a beam current of 1000 pA.

XPS measurements were performed on both pristine and cycled electrodes after 280 cycles. The fluorinated and non-fluorinated samples were washed using DMC and EMC, respectively. They were mounted to the sample holder using copper tape on top of polyimide tape, insulating the samples from the spectrometer in a 'floating' configuration. Samples were mounted in an argon glovebox, and the holder sealed and pumped before transferring to a Kratos AXIS Supra+ X-ray photoelectron spectrometer. A monochromated Al K α X-ray source (1486.6 eV) with an X-ray power of 225 W was used for measurements, with the 'slot' collimation and 'hybrid' lens modes. The analysis spot size was approximately 700 \times 300 μ m. The charge neutraliser system was used during measurements with a current of 0.4 A, bias of 0.17 V and charge balance of

0.67 V. A pass energy of 20 eV was used for high-resolution scans.

CasaXPS software was used for spectral analysis with a Shirley background and employing the Gaussian-Lorentzian GL(30) peak shape. Energy calibration was performed using the sp³ carbon (C-C) peak at 285 eV. Probing depths (3 \times IMFP) were calculated using the TPP-M2 equation as detailed in the NIST database, using parameters for polyethylene, as a low-density material representative of the surface layer studied here.^{33,34} The approximate probing depth is estimated as 14 nm. This depth should be considered as an upper limit, since electron kinetic energies are used in calculations, while it should also be noted that a smaller probing depth would be expected for denser inorganic materials, including those making up the bulk electrodes.

Results and discussion

Electrochemical performance

The electrochemical performance of full cells with the NMC622 cathode containing PVdF (NMC622(PVdF)) and the Si-graphite anode, using a fluorinated electrolyte based on LiPF₆ and a fluorine-free electrolyte based on LiBOB, is shown in Fig. 1. In the first formation cycle at C/20, the NMC622(PVdF)||Si-graphite cell with highly fluorinated and fluorine-free electrolytes delivered similar discharge capacities of 2.0 mA h cm⁻² with initial coulombic efficiencies of 79.2% and 79.5%, respectively. In terms of long-term cycling, the coulombic efficiency remained stable and above 99.8% and the capacity retentions for the fluorinated and fluorine-free systems were 56.2% and 58.3%, respectively, after 500 cycles at a C/2 rate (Fig. 1a and b). While the difference in cycling stability is small for the fluorinated electrolyte cell compared to the previous publication with NMC111 and the same anode,²⁷ the cycling stability of the cells with the fluorine-free electrolyte is clearly improved. For the NMC111||Si-graphite system, the capacity retentions for fluorinated and fluorine-free electrolytes after 300 cycles at C/2 rate were 78.5% and 59.4%, respectively; and for the current systems they are 83.4% and 80.9%, respectively. In the literature, the degradation of LiBOB is often considered one of the main reasons for capacity fading.^{25,26} However, despite using the same anode and electrolyte as in the previous paper, a significant improvement in capacity retention was observed.

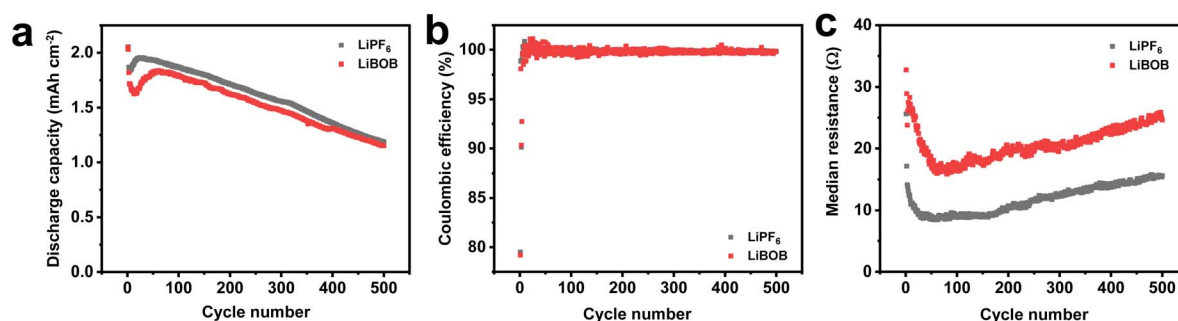


Fig. 1 Electrochemical performance of NMC622(PVdF)||Si-graphite cells cycled at C/2 between 3.0 and 4.2 V with fluorinated (black) and fluorine-free electrolytes (red). (a) Discharge capacity, (b) coulombic efficiency and (c) median resistance vs. cycle number.



These results suggest that the cathode limited the performance of the fluorine-free electrolyte in the case of NMC111||Si-graphite and it improved with the next-generation cell composed of NMC622(PVdF)||Si-graphite. Furthermore, the obtained capacity retention for both electrolyte systems, using high-mass-loading and high-energy-density electrodes, exceeds previously reported values for NMC||Si-based full cells.^{35–37} These results confirm the potential of this fluorine-free electrolyte and the importance of optimizing all the battery components.

The evolution of cell resistance with the two electrolytes was monitored using the intermittent current interruption (ICI) technique.^{31,32} The median cell resistance is higher throughout the long-term cycling for the cell with the fluorine-free electrolyte than the one with the highly fluorinated electrolyte (Fig. 1c). The voltage profiles with the two electrolytes are very similar during the formation cycles, except for a short plateau in the first cycle at 1.9 V for the fluorine-free electrolyte from LiBOB decomposition and at 2.5 V for the fluorinated electrolyte from the FEC decomposition³⁸ (Fig. S1). The resistance evolution during this first cycle is higher for the cell with the fluorine-free electrolyte, indicating contributions from the LiBOB-based decomposition products. The voltage profiles during cycling at C/2 are also similar throughout the cycling, except for the initial stabilization cycles when the capacity drops slightly and is soon recovered. This difference is not contributing to the higher resistance of the fluorine-free electrolyte because the median resistance decreases with both electrolytes. Despite the overall higher cell resistance with LiBOB-based electrolyte, the resistance evolution is the same in both systems, with a decrease in the initial 50 cycles followed by a steady increase until 500 cycles, indicating that this evolution is related to the active materials and not the electrolyte itself.

To investigate the effect of each electrode, three-electrode cells were assembled with lithium metal as the reference electrode. As shown in Fig. S1 and mentioned before for the two-electrode cells, the main difference in the voltage profiles of the first formation cycle at C/20 appears as a short plateau at low voltages. This can be observed in the corresponding derivative of capacity with respect to full-cell voltage (dQ/dV) plots for the full cell and each electrode (Fig. S1d–f). The full cell with the fluorinated electrolyte featured a peak at around 2.5 V, corresponding to a peak in the negative electrode at 1.3 V vs. Li^+/Li , indicating the reduction of the additives FEC/VC. In the case of the cell with the fluorine-free electrolyte, there is a peak at 1.9 V, which also corresponds to a peak for the negative electrode at 1.8 V vs. Li^+/Li , indicating the reduction of LiBOB.²⁶ Similar peaks were observed in the full cell of NMC111||Si-graphite,²⁷ suggesting that they originate from the negative electrode, as that is the electrode in common, due to the formation of the SEI layer.

Fig. S2 compares the rate capability of full cells using fluorinated and non-fluorinated electrolytes from C/20 to 2C. At low C-rates below 1C, the electrochemical performance between the two systems is very similar. Increasing the C-rate results in a lower coulombic efficiency in the first cycle that is recovered in the following ones. However, that is not the case at 2C; the decrease in coulombic efficiency is more abrupt and not

recovered in the following cycles, indicating the presence of parasitic reactions, more evident for the cell with the fluorine-free electrolyte. The discharge capacity also decreases at higher C-rates (1C and 2C) for both cells and an initial increase in resistance is observed at 2C that decreases in the following cycles. However, the limited capacity at high C-rates for the fluorine-free electrolyte might be due to its lower ionic conductivity. Furthermore, the capacity at C/2 was not fully recovered after the C-rate test for the two cells showing 97.9% and 95.8% capacity retention with the fluorinated and fluorine-free electrolytes, respectively. This trend indicates parasitic reactions and relatively slow Li^+ transport occurring during cycling, which limit these systems at high C-rates and are more pronounced with the fluorine-free electrolyte.

Despite the promising results observed from the long-term cycling at C/2 with the fluorine-free electrolyte, the cathode still contains a fluorinated PVdF binder (PFAS source) processed with NMP. To further improve the sustainability of these systems, the PVdF binder was replaced with fluorine-free, water-processable binders, such as a mixture of CMC and latex.

Fig. 2 shows the performance of these two electrolytes in cells containing an aqueous-processed NMC622 cathode with the same silicon-graphite anode. Both cells delivered initial discharge capacities of 1.55 and 1.48 mA h cm^{-2} at C/2 rate after the formation cycles at C/20 for fluorinated and fluorine-free electrolytes, respectively (Fig. 2a). After 500 cycles, the capacity retention was 65% and 61% for the fluorinated and fluorine-free cells, respectively, and the coulombic efficiencies were above 99.8% for both cells (Fig. 2b). The cell resistance follows the same trend as with the PVdF-based cathodes, a decrease in the initial 50 cycles and then a continuous increase for the following 500 cycles. However, the resistance values are slightly higher for the aqueous-processed cathode with both electrolytes, and higher for the cell with the fluorine-free electrolyte compared to the cell with the highly fluorinated one (Fig. 2c). Overall, despite the lower discharge capacity of the aqueous-based electrodes, the capacity retention was slightly higher (61–65%) than with the PVdF-based cathode (56–58%) after 500 cycles, indicating that the fluorine-free electrolyte is also a promising alternative for aqueous-processed cathodes. Moreover, to compare SEI layer formation, the voltage profiles and corresponding derivatives of capacity from two-electrode cells with aqueous-processed cathodes are presented in Fig. S3a and b, respectively. Similar peaks are observed in both fluorinated and fluorine-free electrolytes, corresponding to the decomposition of FEC and LiBOB in cycled cells respectively, confirming the formation of a similar SEI layer with both electrodes.

Surface morphology and elemental mapping analysis

To further analyze the contribution of the electrolytes to the formation of the SEI and CEI layers and to understand how cycling affects their properties, we studied the morphology and elemental mapping of the electrodes in their pristine state and after 280 cycles using SEM and EDS.



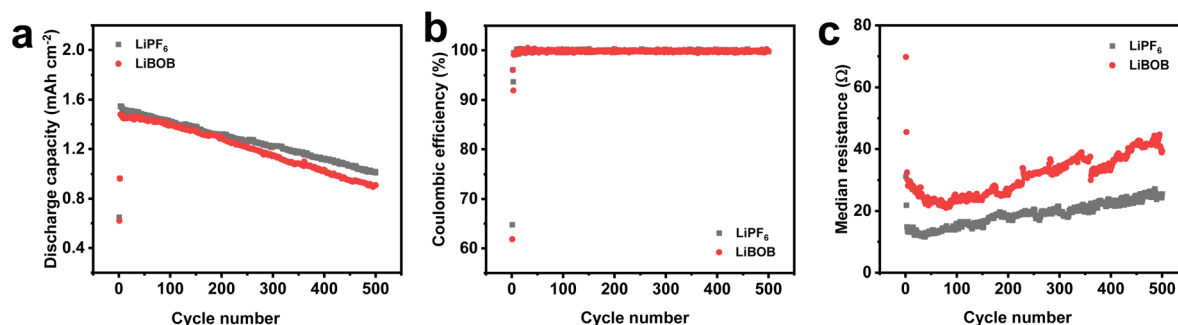


Fig. 2 Electrochemical performance of NMC622(aqueous)||Si-graphite cells cycled at C/2 between 3.0 and 4.2 V with fluorinated (black) and fluorine-free (red) electrolytes. (a) Discharge capacity, (b) coulombic efficiency and (c) median resistance during discharge vs. cycle number.

SEM images of the pristine and cycled electrodes with fluorinated and fluorine-free electrolytes are presented in Fig. 3. The anode is composed of silicon particles distributed homogeneously over larger graphite particles. Fig. 3a and d show the same silicon-graphite pristine anode at two different magnifications, focusing on the graphite and the silicon particles, respectively. The large particles in the range of 20–30 μm correspond to graphite, while the smaller particles, in the range of 0.5–3 μm , correspond to silicon.^{27,39} The change in morphology of the anodes extracted from the cells containing PVdF-based cathodes, cycled in fluorinated and fluorine-free electrolytes, can be seen in Fig. 3b and c, respectively. Graphite particles cycled with the fluorinated electrolyte do not show significant differences compared to the pristine anode; however, with the fluorine-free electrolyte, the graphite particle surface appears slightly smoother.^{28,40} In both electrolytes, the silicon particles remain homogeneously distributed over the

electrode but they are larger and seem to be less compact, exhibiting a rough, coarsely vesicular appearance. In the case of the fluorine-free electrolyte, more agglomeration of the silicon particles can be observed. The corresponding morphologies of the anode materials extracted from the cells containing aqueous-processed cathodes are presented in Fig. 3e and f for the fluorinated and fluorine-free electrolytes, respectively. With the fluorine-free electrolyte, the graphite particles show similar morphology regardless of the cathode used in the cell. However, with the fluorinated electrolyte and the aqueous-processed cathode, the graphite particles show a rough surface (Fig. 3e) not seen when cycled with the PVdF-based cathode (Fig. 3b). A similar morphology evolution is observed for the silicon particles, with an increase in the particle size during cycling and less agglomeration with the fluorine-free electrolyte. The enhancement of Si particle size can be attributed to the formation of the SEI layer and the volume changes during cycling. The more pronounced change in surface morphology for the anode, especially of the silicon particles, cycled with the fluorine-free electrolyte, regardless of the cathode used, could also explain the higher resistance observed during cycling with both cathodes.

The morphological evaluations of the cathodes were conducted for the two types of NMC622 electrodes, with PVdF and aqueous-processed binders, and are shown in Fig. 3g–i and j–l, respectively. The particle size of NMC622 is 10–15 μm with a granular structure on the surface for both pristine electrodes. For both sets of cathodes, cycled with fluorinated and fluorine-free electrolytes (Fig. 3h, i and k, l, respectively), morphology changes are observed on the surface, although the granular structure remains visible. These results suggest the formation of a CEI layer during cycling with both electrolytes on both cathodes. Furthermore, the aqueous-processed NMC622 shows particle coverage from the conductive carbon and binder, which has been previously reported with similar electrode processing.^{13,41} This observation explains the lower discharge capacity observed with the aqueous-based NMC622 and higher cell resistance.

Elemental mapping of the pristine electrodes and after 280 cycles with fluorinated and fluorine-free electrolytes was done with EDS analysis. As shown in Fig. 4, for the anode electrodes extracted from the cells with aqueous-processed cathode, there

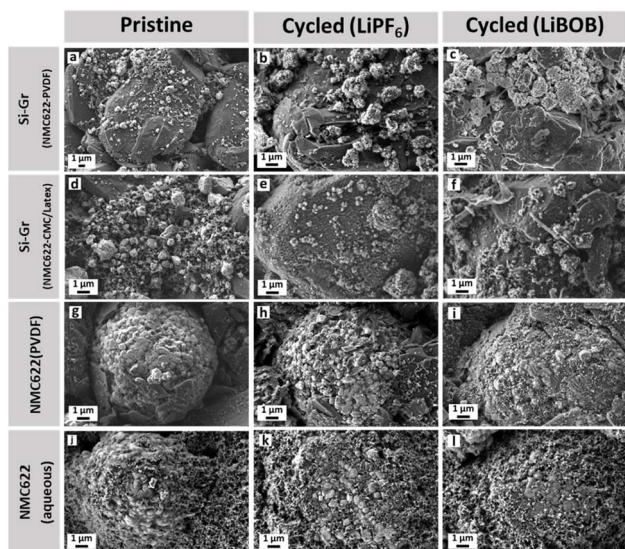


Fig. 3 SEM images of (a, d, g and j) pristine electrodes and after 280 cycles with (b, e, h and k) fluorinated and (c, f, i and l) fluorine-free electrolytes. (a and d) Pristine Si-graphite at different magnifications and extracted from the cells containing (b and c) NMC622(PVdF) and (e and f) NMC622(aqueous) cathodes. Corresponding images of the (g–i) NMC622(PVdF) and (j–l) NMC622(aqueous) cathodes.



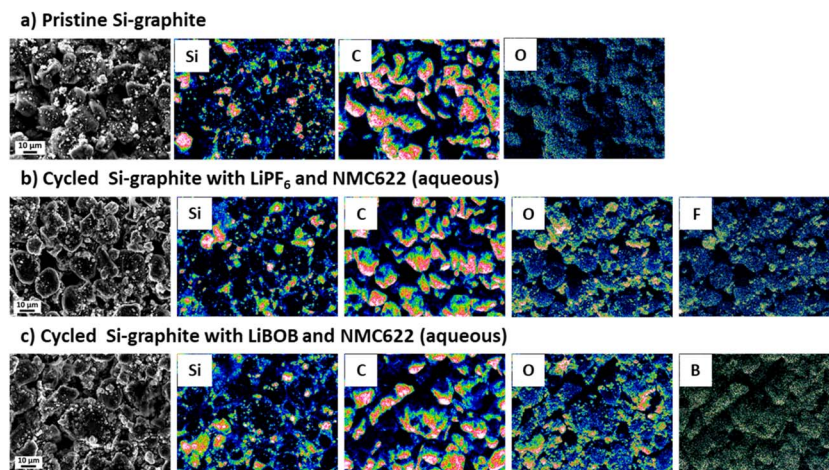


Fig. 4 SEM images and elemental mapping of the silicon-graphite composite (extracted from the cells containing NMC622(aqueous)): (a) pristine and after 280 cycles with (b) fluorinated and (c) fluorine-free electrolytes. The intensity of each element is color coded, ranging from black/blue for low intensity to pink/white for higher intensity.

was an increase in the oxygen content from 3.6% in the pristine sample (mainly from the LiPAA binder and native oxide on Si particles) to 16.0% after cycling with the fluorinated electrolyte, likely due to the decomposition of the solvent and/or additives. The corresponding value for the anode cycled with the fluorine-free electrolyte is higher, 23.5%, suggesting the additional decomposition of the BOB anion, as observed in previous studies.^{19,28} The elemental mapping of fluorine (F) in the cell with the fluorinated electrolyte (Fig. 4b) shows higher intensity on the silicon particles compared to the graphite particles, indicating a preferential decomposition of the electrolyte on the silicon. In contrast, in the cell with the fluorine-free electrolyte (Fig. 4c), there is a strong correlation between boron (B) and carbon (C), indicating that boron preferentially deposits on graphite particles.²⁸ However, the oxygen distribution seems to cover both types of particles without a clear preference for silicon or graphite. A similar elemental mapping trend in the

case of the fluorine and boron distributions can be observed on the anodes extracted from the cells with PVdF-based cathodes (Fig. S4). However, lower oxygen content is observed, 11.0% and 21.4%, for the fluorinated and fluorine-free electrolytes, respectively, compared to the anode from the aqueous-processed cathode. These results show that changing the cathode formulation (binder and solvent used during processing) influences the electrolyte decomposition and SEI layer on the anode side towards a more oxygen-rich SEI with aqueous-processed fluorine-free cathodes.²⁹

Fig. 5 shows the elemental mapping for the aqueous-processed cathode. As expected, the pristine sample lacks F, but in the cycled sample with the fluorinated electrolyte, its content increases to 5.9% indicating the decomposition of the salt and/or FEC additive. On the other hand, the oxygen content changes from 18.3% in the pristine sample to 16.4% and 19.7% in the cycled samples with fluorinated and fluorine-free

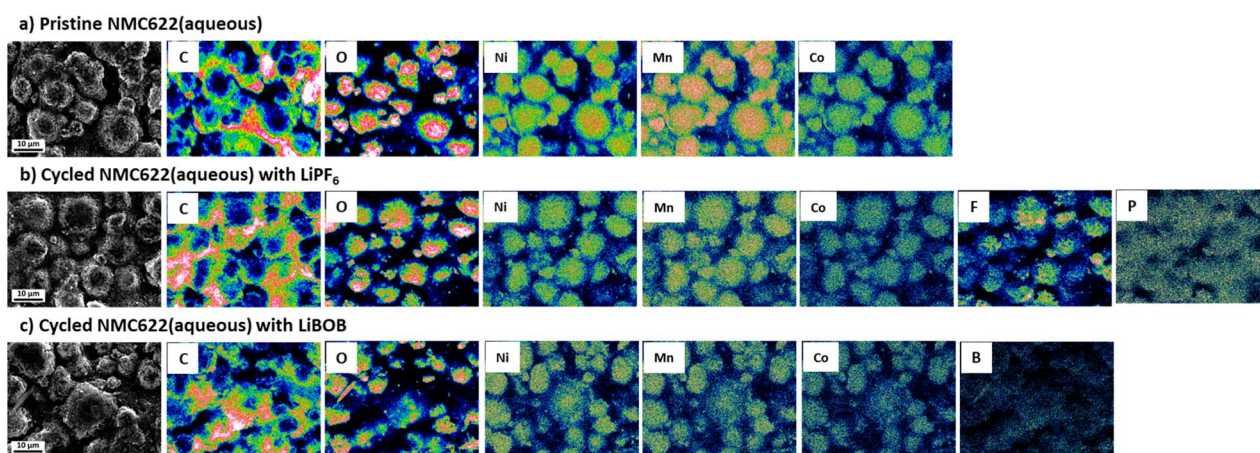


Fig. 5 SEM images and elemental mapping of the NMC622(aqueous) cathode: (a) pristine and after 280 cycles with (b) fluorinated and (c) fluorine-free electrolytes. The intensity of each element is colour coded, ranging from black/blue for low intensity to pink/white for higher intensity.



electrolytes, respectively. The decrease in oxygen for the fluorinated cell indicates the presence of a fluorine-rich CEI layer covering the cathode's surface and burying the oxygen contribution. The increase in oxygen with fluorine-free electrolyte is attributed to the decomposition of BOB anion on the cathode's surface.⁴² Furthermore, the fluorine distribution is predominantly located on the active material particles whereas the boron distribution seems to follow where the carbon black/binder is, mirroring the correlation between B and C on the anode. Fig. S5 shows the elemental mapping of the PVdF-based cathode electrodes. The oxygen content increases slightly after cycling, from 16.3% in the pristine cathode to 16.8% and 18.5% in the cycled cells with fluorinated and fluorine-free electrolytes, respectively. This indicates that besides the oxygen from the NMC622(PVdF), a CEI layer with oxygen-based species is also formed and to a larger degree with the fluorine-free electrolyte. Fluorine is present in all samples due to the presence of PVdF as a binder in the cathode. As expected, the variation in the amount of fluorine is quite small after cycling with the fluorine-free electrolyte. However, the fluorine content increases when cycled with the fluorinated electrolyte, rising from 2.1% in the pristine cathode to 5.6%, indicating the formation of an F-containing CEI layer from the decomposition of fluorinated components in the electrolyte (salt and/or FEC). Furthermore, the presence of phosphorus corroborates the salt decomposition on the cathode surface. The boron mapping shows a similar trend with the other cathode, with a preferential distribution together with carbon species.

Chemical composition analysis of the interphases

Using SEM for morphological analysis and EDS for elemental mapping provided insights into the surface layers and their compositions as well as the effect of different electrolytes and cathode formulations on such surfaces. To complement this, XPS analysis was employed to provide more information about

the chemical composition and environment of the surface of electrodes and the CEI and SEI layers after 280 cycles.

Cathodes. Fig. 6 shows the C 1s and O 1s spectra of PVdF- and aqueous-processed NMC622 electrodes, respectively, in their pristine state and after 280 cycles with fluorinated and fluorine-free electrolytes, obtained from full cells of NMC622||Si-graphite. The corresponding positions of the deconvoluted peaks are provided in Table S1. By analyzing the relative peak intensities of the C=C peak in the C 1s spectra (Fig. 6a and c) and the M-O peak in the O 1s spectra (Fig. 6b and d) of both pristine and cycled samples – which originate from carbon black and metal oxides, respectively – the thickness of the CEI layers can be evaluated. For the PVdF-based cathode, the relative peak intensity of C=C decreases after cycling for both electrolytes, although to a larger extent with the fluorine-free electrolyte, suggesting a thicker CEI with this electrolyte. In addition, the relative peak intensity of M-O in the pristine sample is almost completely diminished after cycling with both electrolytes, indicating that a CEI layer has formed over the cathode active material.

In the C 1s spectra of NMC622(PVdF), the presence of the PVdF binder can be identified through the CH₂ (PVdF) and CF₂ (PVdF) groups in the pristine electrode. After 280 cycles in both electrolytes, the PVdF peaks persist, and the corresponding signal in the F 1s spectra confirms this as well (Fig. S6). Notably, the single F 1s peak observed in the fluorine-free sample further confirms that any detected fluorine originates from the binder in that system. However, upon cycling, newly formed carbonate and ether species begin to overlap with the CH₂ (PVdF) and CF₂ (PVdF) peaks. As a result, the apparent increase in intensity at these binding energies reflects not only the presence of the PVdF binder but also the CEI layer growth.

Upon cycling, the relative peak intensities of ether (C-O), carbonyl (C=O), ester (O=C-O) and carbonate (CO₃) groups increase compared to the pristine electrode (where any such

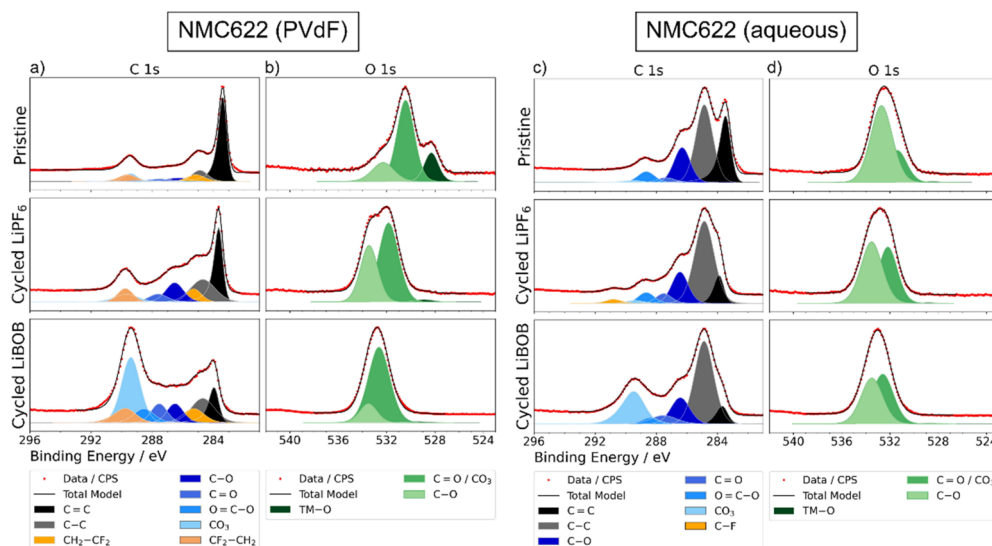


Fig. 6 XPS (a and c) C 1s and (b and d) O 1s spectra of NMC622(PVdF) and NMC622(aqueous) cathodes, respectively: pristine (top row) and after 280 cycles using fluorinated (middle row) and fluorine-free (bottom row) electrolytes.



peaks likely come from surface groups on the conductive carbon additive or the cathode material), again confirming the decomposition of the solvent and/or additives on the cathode surface to form the CEI layer. This CEI layer includes Li_2CO_3 , ROLi , and ROCO_2Li (R: alkyl group) coming from the interaction between the cathode and the electrolyte components.⁴³

A key difference between the fluorinated and fluorine-free electrolytes is the relative peak intensity of the carbonate group, which is much larger in the latter electrolyte. Furthermore, the appearance and noticeable contribution of the ester group in the cycled sample with the fluorine-free electrolyte might originate from the decomposition of the electrolyte components or could simply be residual LiBOB salt (from the oxalate groups) remaining in the CEI layer or trapped in the electrode's porous structure after washing with EMC. Although gas evolution was not observed in the cycled pouch cells, CO_2 evolution from LiBOB decomposition has been investigated with mass spectrometry.^{44,45} However, the released CO_2 can react further with EC forming polycarbonate-like oligomers, which could explain the high concentration of carbonates seen in this study when using LiBOB as the main salt and not only as an additive.⁴⁶

The O 1s spectra can be resolved into three peaks: transition metal oxide (M–O), $\text{C}=\text{O}/\text{CO}_3$, and C–O. It can be observed that the cycled samples exhibit peaks that shift to higher binding energies, likely due to changes in the chemical environment caused by surface reactions and the formation of a CEI layer.⁴⁷ In the O 1s spectra of the PVdF-based cathode (Fig. 6b), in addition to the decrease in the M–O peak with both electrolytes, an increase in the $\text{C}=\text{O}/\text{CO}_3$ and C–O peaks is observed, suggesting the formation of the CEI layer from electrolyte decomposition products. The fluorinated electrolyte leads to a mixture of $\text{C}=\text{O}/\text{CO}_3$ and C–O-based species, while with the fluorine-free electrolyte, the CEI layer is mainly composed of carbonate species as indicated by the large peak in both C 1s and O 1s spectra.

The O 1s spectrum of the pristine aqueous-processed cathode (Fig. 6d) displays oxygen-containing groups – namely, C–O, $\text{C}=\text{O}$, and $\text{O}-\text{C}=\text{O}$ – which correspond to the binder (CMC and latex). The low relative intensity of the TM–O peak in the pristine O 1s spectrum indicates that the NMC particles are completely covered by the binder and conductive additive, whose thickness exceeds the probing depth of XPS of ~ 14 nm (estimated from the Al K α kinetic energy, see the Experimental section), as also observed in the SEM images (Fig. 5j), in contrast to the cathode with the PVdF binder. Therefore, this peak cannot be used to compare the CEI thicknesses. However, the persistent $\text{C}=\text{C}$ signal in the C 1s spectrum from the conductive additives suggests a thinner or more porous binder coating on the conductive additive, allowing to compare the CEI layer thickness with cycling. The fact that the $\text{C}=\text{C}$ peak remains observable confirms that the formed CEI layer is also thinner than the XPS probing depth. However, the relative peak intensity of $\text{C}=\text{C}$ decreases slightly more after cycling with the fluorine-free electrolyte, suggesting a slightly thicker CEI compared to the fluorinated electrolyte, similar to the PVdF-based cathodes. Furthermore, upon cycling, the ester peak

grows and the carbonate peak appears, with a higher contribution in the sample cycled with the fluorine-free electrolyte. This correlates with the C 1s spectra in the PVdF-based cathode, although the relative intensity of the carbonate peak with the fluorine-free electrolyte is lower with the aqueous-based cathode. These results could be due to the better coverage of the active material preventing to more extent the decomposition from the LiBOB-based electrolyte. F 1s spectra of PVdF and aqueous-based NMC622 are shown in Fig. S6a and b, respectively. For the NMC622(PVdF), the peak at around 687 eV corresponds to CF_2 (PVdF) from the binder in all the samples. Additionally, a LiF peak was observed in both the pristine and fluorine-free samples, possibly coming from the parasitic dehydrofluorination of PVdF.^{48–50} The spectrum after cycling with the fluorine-free electrolyte does not show any additional peaks besides the binder and LiF as also observed in the pristine sample. Clearer changes can be observed after cycling with the fluorinated electrolyte. The LiF peak is dominating the spectrum, followed by organofluorine species and P–F from the presence or decomposition of LiPF_6 . For the aqueous-based NMC622, the F 1s spectra show no fluorine present in either the pristine sample or the sample cycled with the fluorine-free electrolyte. However, the F 1s spectrum (Fig. S6b) of the cathode cycled with the fluorinated electrolyte exhibits the presence of LiF (to a lower extent), P–F, and other organofluorine compounds, most likely from the FEC additive, confirming a fluorine-rich CEI layer.

In the P 2p spectra (Fig. S7a and b) for PVdF- and aqueous-based NMC622, cycling with the fluorinated electrolyte leads to the appearance of three peaks, assigned to PO_4 , PO_xF_y , and PF_6^- compounds. Each peak splits into two components due to spin–orbit coupling, with a separation of 0.84 eV. These peaks indicate the decomposition of the LiPF_6 salt as well as possible residual salt that was not completely rinsed off from the electrode during washing with DMC.⁴⁷ The P 2p spectrum of NMC622(aqueous) shows a larger contribution of phosphate-based decomposition products from LiPF_6 , and also residual LiPF_6 salt compared to NMC(PVdF). The lower contribution from LiF and higher P–F in the F 1s spectrum as well as higher PF_6^- in the P 2p spectrum with aqueous-based NMC622 suggest less salt decomposition compared to the PVdF-based cathode, which could be due to the better coverage of the active material in the former electrode by the binder and carbon additives, as seen with the fluorine-free electrolyte.

The Li 1s spectra of PVdF and aqueous-based NMC622 are shown in Fig. S8a and b, respectively. For both cathodes, in the Li 1s spectra, the pristine one displays a single peak, corresponding to TM–Li which diminishes in the cycled sample with fluorinated and fluorine-free electrolytes, respectively. The dominant peak in the cycled samples is near 55 eV arising from Li_2CO_3 peaks; however, in the fluorinated electrolyte this peak also contains overlapping contributions from LiF and $\text{Li}_x\text{PO}_y\text{F}_z$ (from LiPF_6/FEC decomposition), which have very similar binding energies in the Li 1s region.

The B 1s spectra in Fig. S9a and b for NMC622(PVdF) and NMC622(aqueous), respectively, from cycled sample with the fluorine-free electrolyte confirm the presence of boron-based



species on the surface indicating residues and/or decomposition of the LiBOB salt. The B 1s spectrum can be deconvoluted into two peaks: one originating from B–O bonds formed by LiBOB decomposition on the cathode, and the other at higher energy from oxalate groups of the BOB anion that remain adsorbed on the electrode surface.⁵¹ The higher relative intensity of BOB to B–O in the aqueous-based NMC622 cathode compared to the PVdF-based cathode indicates less salt decomposition in agreement with the other spectra.

Overall, from the XPS analysis of the PVdF- and aqueous-processed NMC622, a complete coverage of the active material particles is observed with the aqueous-processed (CMC-latex) formulation. While this can contribute to the higher cell resistances and lower discharge capacity observed with this cathode, the capacity retention is slightly higher. These results indicate that the coverage of the cathode particles contributes to the resistance but at the same time prevents electrolyte decomposition to a greater extent compared to the uncovered particles in the PVdF-based cathode. Furthermore, more carbonate species are observed on the NMC622(PVdF) surface than on the aqueous-processed NMC622 surface with both electrolytes, although to a larger extent with the fluorine-free electrolyte. Salt decomposition from the presence of phosphate and boron-based species is detected in all cells. Comparing the two electrolytes, a thicker layer is observed with the LiBOB-based electrolytes which correlates with the higher resistance seen with this electrolyte already in the first cycle with both types of cathode formulations.

Anodes. The C 1s and O 1s spectra of the silicon-graphite anode electrode, pristine and cycled against NMC622(PVdF) and NMC622(aqueous), are shown in Fig. 7. In the C 1s spectra of the pristine sample (Fig. 7a), the largest components are C–C, C=C and C=O–O. C–C mostly originates from the binder (LiPAA), graphite and carbon black. The C=C bond component can be attributed to graphitic carbon from graphite and carbon

black. The other peak attributed to C=O–O mainly comes from the LiPAA binder. The other bonds, C–O, C=O, and CO₃ come from the surface species from graphite, carbon black, and the binder.²⁷

The cycled samples show a significant decline in the peak intensity for the C=C, indicating the formation of the SEI layer. However, the continued visibility of the C=C peak in all cycled samples indicates that the SEI layer thickness does not exceed the XPS probing depth. Moreover, analysis of the Si 2p spectra (Fig. S10) shows a clear Si signal in the anode samples – most pronounced in those paired with the PVdF-based cathode. Given the XPS probing depth of approximately 14 nm, this confirms that the SEI layer thickness is around 14 nm.

The remaining components with different relative intensities in the C 1s spectra C–O, C=O, O=C–O, and CO₃ arise from lithium alkoxides (ROLi), lithium alkyl carbonates (ROCO₂Li), and Li₂CO₃, all formed by decomposition of the electrolyte during cycling.⁵² The partially lithiated phase of carbon leads to the formation of Li_xC²⁷ and the C–F peak appears only for the fluorinated electrolyte.

The C 1s and O 1s spectra of the anode electrode cycled against the PVdF-based cathode with the fluorinated electrolyte show an increase in C–O compared to the pristine anode, which is attributed to the decarboxylation of the carbonate solvents and/or additives.⁵³ With the fluorine-free electrolyte, the main peaks correspond to ester and carbonate species followed by C–O. This is indicative of BOB anion decomposition leading to oxalates (esters)^{28,44} and carbonates from solvents and the VC additive.⁴⁰ In the case of the O 1s spectrum, the fluorine-free electrolyte shows an additional peak corresponding to OH, observed previously for the same anode and electrolyte.²⁷ Different features are observed when the anode is cycled against the aqueous-based cathode. With the fluorinated electrolyte, there is a large contribution from C=O and C–F species and to a minor degree C–O species. The C–F bond at a high binding

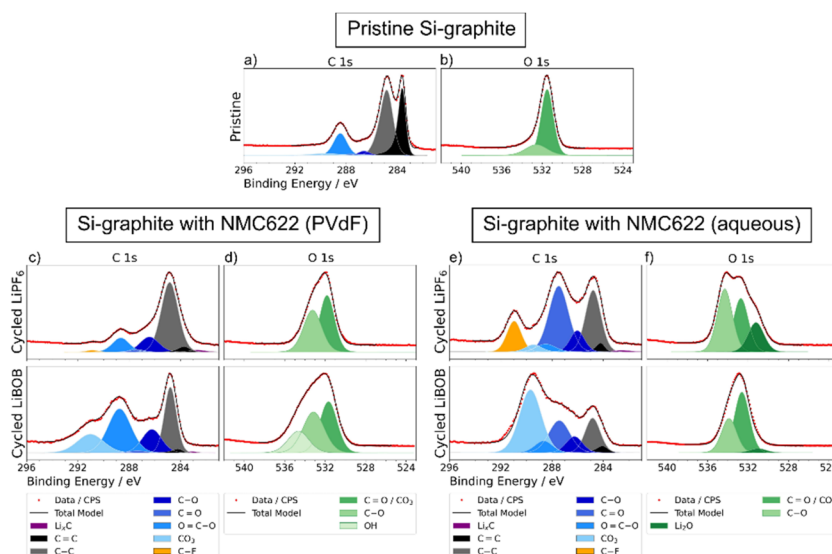


Fig. 7 XPS (a, c and e) C 1s and (b, d and f) O 1s spectra of Si-graphite anodes, pristine (top row) and after 280 cycles with NMC622(PVdF) and NMC622(aqueous), respectively, using fluorinated (middle row) and fluorine free (bottom row) electrolytes.



energy arising from organic fluorinated species most likely comes from the reduction of FEC.⁵⁴ The O 1s spectrum shows a relatively intense peak attributed to Li₂O observed previously with silicon electrodes.^{40,55,56}

The anode cycled in the fluorine-free electrolyte features mainly carbonates, followed by C=O and esters most likely from LiBOB and VC/solvent decomposition or LiBOB residues remaining on the electrode after washing with EMC.²⁸ Li₂O is also present in the O 1s spectrum although to a much lower degree compared to the fluorinated electrolyte.

The F 1s spectra of anodes cycled with the fluorinated electrolyte with NMC622(PVdF) and NMC622(aqueous) are shown in Fig. S11a and b, respectively. In both cases, they are dominated by LiF, although there are other minor components assigned to organofluorine compounds, and P–F, coming from the degradation of the FEC additive and the LiPF₆ salt on the anode surface.⁵⁷ The corresponding P 2p spectra (Fig. S12) show different phosphate peaks, confirming that the SEI layer with the fluorinated electrolyte contains inorganic species from salt decomposition and LiPF₆ salt remaining on the anode. As shown in Fig. S11b and S12b, the F 1s and P 2p spectra of the anode cycled with the fluorinated electrolyte and NMC622(aqueous) cathode contain larger contributions from PF₆[−] and organofluorine compounds, compared to the anode cycled with the NMC622(PVdF) cathode that mainly contains LiF and PF_xO_y. This suggests more salt decomposition on the anode when cycled with NMC622(PVdF).

The B 1s spectra of Si-graphite electrodes cycled in the fluorine-free electrolyte from cells with PVdF-based cathodes (Fig. S13a) and aqueous-processed cathodes (Fig. S13b) show the presence of B–O and BOB[−] species. The B 1s spectrum can be deconvoluted into two peaks: one originating from B–O bonds formed by LiBOB decomposition on the anode, and the other from oxalate groups of the BOB anion that remain adsorbed on the electrode surface. These could come from LiBOB salt residues and/or decomposition of LiBOB on the anode side with higher relative intensity of the latter when paired with NMC622(PVdF).⁵⁸ This follows the same trend as with the fluorinated electrolyte, with less salt degradation for the aqueous-based NMC622.

Overall, fluorine-free electrolytes form an oxygen-rich SEI layer on the anode composed of carbonates, esters and ether species in different ratios as previously reported.²⁷ In addition, these results show different electrolyte decomposition mechanisms on the anode depending on the cathode's formulation. More salt decomposition is observed on the anode when cycled with NMC622(PVdF), as seen from the higher relative intensity of PF_xO_y and B–O species for each electrolyte. In contrast, with the fluorinated electrolyte, more decomposition products from the solvent and additives are observed in the C 1s and O 1s spectra on the anode cycled with NMC622(aqueous) forming C–F, C=O and Li₂O products. With the fluorine-free electrolyte, it is the ratio of the decomposition products that is the main difference between the two cells with the different cathode formulations. The one with NMC622(PVdF) shows a higher contribution from ester compared to carbonates, which has been previously assigned to LiBOB decomposition and VC being

unable to protect the silicon electrode fully.⁴⁰ When cycled with NMC622(aqueous), a higher contribution from carbonate species is observed, which is assigned to VC decomposition and therefore prevents, to some degree, LiBOB decomposition resulting in a better SEI. These results correlate with the improved cycling stability, and higher capacity retention, as reported previously with silicon wafers.⁴⁰

In summary, the LiBOB-based electrolyte mainly forms carbonate species on the cathode's surface regardless of its composition and a slightly thicker CEI compared to the LiPF₆-based electrolyte. Between the PVdF- and aqueous-processed cathodes, the better coverage of the latter seems to prevent electrolyte decomposition to a larger extent, influencing the SEI layer on the anode. The higher intensity of the carbonate peaks with the fluorine-free electrolyte and NMC622(aqueous) also suggests a better SEI formed from the VC additive instead of LiBOB decomposition. These results agree with the higher capacity retention observed with the fluorine-free aqueous-based NMC622 cathode. Furthermore, the similar cycling stability obtained with the two electrolytes confirms the potential competitiveness of fully fluorine-free lithium-ion batteries, contributing to lower toxicity and greater sustainability.

Conclusion

The effect of fluorine-free components in the electrolyte and binder in full cells containing a silicon-graphite composite anode and NMC622 cathode was investigated. Long-term galvanostatic cycling at C/2 showed that the fluorine-free electrolyte can perform comparably to state-of-the-art fluorinated electrolytes with a capacity retention of 56.2% and 58.3%, respectively, after 500 cycles. The capacity retention increased when using an aqueous-processed fluorine-free binder (CMC-latex) in the cathode, reaching 61% and 65% after 500 cycles for the fluorine-free and fluorinated electrolytes, respectively. Despite the similar capacities, cell resistance measurements using the intermittent current interruption technique revealed slightly larger values for the cells cycled with the aqueous-processed cathodes and the fluorine-free electrolytes compared to the highly fluorinated electrolyte and binder. Furthermore, the rate capability measurements showed that increasing the C-rate to 2C limits the performance of both cells, with the performance deterioration being relatively more pronounced with the fluorine-free electrolyte.

Surface analysis by SEM, EDS, and XPS was performed on the pristine and cycled samples after 280 cycles. The basic morphology of both electrodes remained well-preserved after cycling with both electrolytes; however, interfacial layer coverage can be seen on both electrodes, which is attributed to the electrolyte decomposition forming the SEI and CEI layers. On the cathode side, the fluorine-free electrolyte decomposed, forming more carbonate-based species than the fluorinated electrolytes, regardless of the cathode's formulation. The coverage of the active material with CMC-latex and aqueous-based processing increases cell resistance but prevents electrolyte decomposition. On the anode side, a preferential



decomposition of the fluorinated electrolyte was observed on the silicon particles while LiBOB preferentially decomposed on the graphite particles. Furthermore, the SEI composition was different depending on the cathode's formulation. With the aqueous-based cathode, less salt decomposition was observed on the anode with both electrolytes. In particular, with the fluorine-free electrolyte a preferential decomposition of VC on the anode surface prevented the LiBOB decomposition, improving the cycling stability.

In conclusion, these results demonstrate that the high-energy-density full cells (NMC622||Si-graphite) with PFAS-free binders and a fluorine-free electrolyte could perform as well as highly fluorinated cells. This study serves as a proof of concept and paves the way towards more environmentally friendly, high-energy-density, and safer lithium-ion batteries.

Author contributions

Conceptualization: G.H.; data curation, analysis, investigation, validation and visualization: G. H., S. M. and A. J. N.; funding acquisition: J. M.; project administration: G. H. and J. M.; supervision: G. H.; writing – original draft: G. H. and S. M.; review & editing: S. M., A. J. N., J. M. and G. H.

Conflicts of interest

There are no conflicts to declare.

Data availability

The data presented in this article are in the form of figures. The data supporting this article have been included as part of the supplementary information (SI). Supplementary information is available. See DOI: <https://doi.org/10.1039/d5ta06760j>.

Acknowledgements

The authors would like to thank VARTA Innovation GmbH for kindly providing NMC622-PVdF and Si-graphite electrodes and CEA-Liten for kindly providing NMC622 aqueous-processed electrodes. The authors acknowledge the financial support from the ECO2LIB project (European Union H2020 research and innovation programme under grant agreement No. 875514). COMPEL and the Swedish strategic research programme STandUP for Energy are acknowledged for financial support. The authors acknowledge Myfab Uppsala for providing facilities and experimental support. Myfab is funded by the Swedish Research Council (2020-00207) as a national research infrastructure.

References

- 1 S. Duehnen, J. Betz, M. Kolek, R. Schmich, M. Winter and T. Placke, *Small Methods*, 2020, **4**, 2000039.
- 2 A. Rensmo, E. K. Savidou, I. T. Cousins, X. Hu, S. Schellenberger and J. P. Benskin, *Environ. Sci.: Processes Impacts*, 2023, **25**, 1015–1030.
- 3 F. Spyraakis and T. A. Dragani, *Toxics*, 2023, **11**, 721.
- 4 T. F. Burton, J. L. Gómez Urbano, Y. Zhu, A. Balducci and O. Fontaine, *Nat. Commun.*, 2025, **16**, 5957.
- 5 K. S. Teoh, M. Melchiorre, S. Darlami Magar, M. Hermesdorf, D. Leistenschneider, M. Oschatz, F. Ruffo, J. L. Gómez Urbano and A. Balducci, *Adv. Mater.*, 2024, **36**, 2310056.
- 6 S. Lander, M. Vagin, V. Gueskine, J. Erlandsson, Y. Boissard, L. Korhonen, M. Berggren, L. Wågberg and X. Crispin, *Adv. Energy Sustainability Res.*, 2022, **3**, 2200016.
- 7 J. Miyake and K. Miyatake, *Polym. J.*, 2017, **49**, 487–495.
- 8 H. J. Lee, H.-S. Jung, J. G. Kim, Y. W. Kim and C. Pak, *ACS Appl. Mater. Interfaces*, 2025, **17**, 5268–5277.
- 9 D. Bresser, D. Buchholz, A. Moretti, A. Varzi and S. Passerini, *Energy Environ. Sci.*, 2018, **11**, 3096–3127.
- 10 R. Shunmugasundaram, R. S. Arumugam, P. Benedek, M. Yarema, P. Baade and V. Wood, *J. Electrochem. Soc.*, 2022, **169**, 60504.
- 11 F. Nagler, N. Christian, A. Gronbach, F. Stahl, P. Daubinger, A. Flegler, M. Hofmann and G. A. Giffin, *ChemElectroChem*, 2024, **11**, e202300748.
- 12 M. Bichon, D. Sotta, N. Dupré, E. De Vito, A. Boulineau, W. Porcher and B. Lestriez, *ACS Appl. Mater. Interfaces*, 2019, **11**, 18331–18341.
- 13 M. Bichon, D. Sotta, E. De Vito, W. Porcher and B. Lestriez, *J. Power Sources*, 2021, **483**, 229097.
- 14 A. C. Rolandi, C. Pozo-Gonzalo, I. de Meatza, N. Casado, M. Forsyth and D. Mecerreyes, *ACS Appl. Energy Mater.*, 2023, **6**, 8616–8625.
- 15 W. Mroziak, M. A. Rajaeifar, O. Heidrich and P. Christensen, *Energy Environ. Sci.*, 2021, **14**, 6099–6121.
- 16 Y. Xu, A. Filippov, M. R. Shimpi, F. Ullah Shah and P. Johansson, *Batteries Supercaps*, 2025, **8**, e202400672.
- 17 P. Jiang, L. Chen, H. Shao, S. Huang, Q. Wang, Y. Su, X. Yan, X. Liang, J. Zhang and J. Feng, *ACS Energy Lett.*, 2019, **4**, 1419–1426.
- 18 Y. Shuai, Y. Hu, X. Gong, Z. Xu, L. Li, L. Zhang, M. Li, J. Zhou and M. Li, *Chem. Eng. J.*, 2025, **505**, 159101.
- 19 G. Hernández, R. Mogensen, R. Younesi and J. Mindemark, *Batteries Supercaps*, 2022, **5**, e202100373.
- 20 F. Wu, A. Mullaliu, T. Diemant, D. Stepien, T. N. Parac-Vogt, J. Kim, D. Bresser, G. Kim and S. Passerini, *InfoMat*, 2023, **5**, e12462.
- 21 T. M. Nguyen, D. W. Kim, D. Y. Kim, G. Choi, J. Suk and Y. Kang, *ACS Appl. Energy Mater.*, 2022, **5**, 15768–15779.
- 22 S. Wen, Y. Han, P. Wang, D. Zhao, X. Cui, L. Zhang and S. Li, *ACS Appl. Energy Mater.*, 2021, **4**, 12525–12534.
- 23 K. Xu, S. Zhang, T. R. Jow, W. Xu and C. A. Angell, *Electrochem. Solid-State Lett.*, 2001, **5**, A26.
- 24 K. Xu, S. Zhang, B. A. Poesse and T. R. Jow, *Electrochem. Solid-State Lett.*, 2002, **5**, A259.
- 25 K. Xu, S. S. Zhang, U. Lee, J. L. Allen and T. R. Jow, *J. Power Sources*, 2005, **146**, 79–85.
- 26 K. Xu, *J. Electrochem. Soc.*, 2008, **155**, A733.
- 27 G. Hernández, A. J. Naylor, Y.-C. Chien, D. Brandell, J. Mindemark and K. Edström, *ACS Sustain. Chem. Eng.*, 2020, **8**, 10041–10052.



- 28 Y.-C. Weng, R. Andersson, M.-T. Lee, J. Mindemark, A. Lindblad, M. Hahlin and G. Hernández, *J. Electrochem. Soc.*, 2024, **171**, 60527.
- 29 R. Gond, H. D. Asfaw, O. Hosseinaei, K. Edstrom, R. Younesi and A. J. Naylor, *ACS Sustain. Chem. Eng.*, 2021, **9**, 12708–12717.
- 30 L. Dettmann, L. O. S. Colbin and A. J. Naylor, *Adv. Mater. Interfaces*, 2025, 2500262.
- 31 M. J. Lacey, K. Edström and D. Brandell, *Chem. Commun.*, 2015, **51**, 16502–16505.
- 32 Y.-C. Chien, H. Liu, A. S. Menon, W. R. Brant, D. Brandell and M. J. Lacey, *Nat. Commun.*, 2023, **14**, 2289.
- 33 C. J. Powell and A. Jablonski, *NIST Electron Inelastic-Mean-Free-Path Database, Version 1.2, SRD 71*, National Institute of Standards and Technology, Gaithersburg, MD, 2010.
- 34 S. Tanuma, C. J. Powell and D. R. Penn, *Surf. Interface Anal.*, 1994, **21**, 165–176.
- 35 M. Gautam, G. K. Mishra, K. Bhawana, C. S. Kalwar, D. Dwivedi, A. Yadav and S. Mitra, *ACS Appl. Mater. Interfaces*, 2024, **16**, 45809–45820.
- 36 N. Hamzelui, M. Linhorst, G. Martin Nyenhuis, L. Haneke, G. G. Eshetu, T. Placke, M. Winter, B. M. Moerschbacher and E. Figgemeier, *Energy Technol.*, 2023, **11**, 2201239.
- 37 S. Hiwase, N. Kumar and M. Furquan, *Chem. Eng. J.*, 2024, **498**, 155085.
- 38 K. Kim, I. Park, S.-Y. Ha, Y. Kim, M.-H. Woo, M.-H. Jeong, W. C. Shin, M. Ue, S. Y. Hong and N.-S. Choi, *Electrochim. Acta*, 2017, **225**, 358–368.
- 39 C. L. Berhaut, D. Z. Dominguez, P. Kumar, P.-H. Jouneau, W. Porcher, D. Aradilla, S. Tardif, S. Pouget and S. Lyonard, *ACS Nano*, 2019, **13**, 11538–11551.
- 40 Z. Lu, T. Patranika, A. J. Naylor, J. Mindemark, S. Tardif, G. Hernández and S. Lyonard, *Small*, 2025, 2410654.
- 41 R. Sahore, D. L. Wood III, A. Kukay, K. M. Grady, J. Li and I. Belharouak, *ACS Sustain. Chem. Eng.*, 2020, **8**, 3162–3169.
- 42 W. Zhao, L. Zou, J. Zheng, H. Jia, J. Song, M. H. Engelhard, C. Wang, W. Xu, Y. Yang and J. Zhang, *ChemSusChem*, 2018, **11**, 2211–2220.
- 43 T. Kim, L. K. Ono and Y. Qi, *J. Mater. Chem. A*, 2023, **11**, 221–231.
- 44 T. Melin, R. Lundström and E. J. Berg, *J. Phys. Chem. Lett.*, 2024, **15**, 2537–2541.
- 45 C. Misiewicz, K. Edstrom and E. J. Berg, *Chem. Mater.*, 2024, **36**, 9729–9740.
- 46 Y. Zhu, Y. Li, M. Bettge and D. P. Abraham, *Electrochim. Acta*, 2013, **110**, 191–199.
- 47 H. Liu, A. J. Naylor, A. S. Menon, W. R. Brant, K. Edström and R. Younesi, *Adv. Mater. Interfaces*, 2020, **7**, 2000277.
- 48 A. M. Andersson, D. P. Abraham, R. Haasch, S. MacLaren, J. Liu and K. Amine, *J. Electrochem. Soc.*, 2002, **149**, A1358.
- 49 K. Edstroem, T. Gustafsson and J. O. Thomas, *Electrochim. Acta*, 2004, **50**, 397–403.
- 50 K. Beltrop, S. Klein, R. Nölle, A. Wilken, J. J. Lee, T. K.-J. Köster, J. Reiter, L. Tao, C. Liang and M. Winter, *Chem. Mater.*, 2018, **30**, 2726–2741.
- 51 E. K. W. Andersson, L.-T. Wu, L. Bertoli, Y.-C. Weng, D. Friesen, K. Elbouazzaoui, S. Bloch, R. Ovsyannikov, E. Giangrisostomi, D. Brandell, J. Mindemark, J. C. Jiang and M. Hahlin, *J. Mater. Chem. A*, 2024, **12**, 9184–9199.
- 52 Y. He, Z. Chen and Y. Zhang, *iScience*, 2024, **27**(8), 110491.
- 53 E. Markevich, G. Salitra and D. Aurbach, *ACS Energy Lett.*, 2017, **2**, 1337–1345.
- 54 S. Ahn, M. Fukushima, H. Nara, T. Momma, W. Sugimoto and T. Osaka, *Electrochem. Commun.*, 2021, **122**, 106905.
- 55 B. Philippe, R. Dedryvère, M. Gorgoi, H. Rensmo, D. Gonbeau and K. Edström, *Chem. Mater.*, 2013, **25**, 394–404.
- 56 C. Cao, I. I. Abate, E. Sivonxay, B. Shyam, C. Jia, B. Moritz, T. P. Devereaux, K. A. Persson, H.-G. Steinrück and M. F. Toney, *Joule*, 2019, **3**, 762–781.
- 57 G. Jiang, J. Liu, J. He, H. Wang, S. Qi, J. Huang, D. Wu and J. Ma, *Adv. Funct. Mater.*, 2023, **33**, 2214422.
- 58 S. Jiao, X. Ren, R. Cao, M. H. Engelhard, Y. Liu, D. Hu, D. Mei, J. Zheng, W. Zhao and Q. Li, *Nat. Energy*, 2018, **3**, 739–746.

